Finite element modelling approach for precast reinforced concrete beam-to-column connections under cyclic loading

Citation for published version:
Feng, D-C, Wu, G & Lu, Y 2018, 'Finite element modelling approach for precast reinforced concrete beam-to-column connections under cyclic loading', *Engineering Structures*, vol. 174, pp. 49-66. https://doi.org/10.1016/j.engstruct.2018.07.055

Digital Object Identifier (DOI):
10.1016/j.engstruct.2018.07.055

Published In:
Engineering Structures

Finite element modelling approach for precast reinforced concrete beam-to-column connections under cyclic loading

De-Cheng Feng[a,b], Gang Wu[a,b,*], Yong Lu[c]

[a] Key Laboratory of Concrete and Prestressed Concrete Structures of the Ministry of Education, Southeast University, Nanjing 210096, China
[b] Laboratory of Industrialized Structural and Bridge Engineering of Jiangsu Province, Southeast University, Nanjing 210096, China
[c] Institute for Infrastructure and Environment, School of Engineering, The University of Edinburgh, Edinburgh EH9 3JL, UK

Abstract

In this paper, a finite element modelling approach is developed for the analysis of the cyclic behavior of precast beam-to-column connections. In particular, the modelling takes into account the compression-softening of concrete, the bond-slip effect in the critical regions and the representation of the post-cast concrete interface. A newly developed softened damage-plasticity model, which can reproduce the typical cyclic behavior of reinforced concrete, is adopted for concrete. Meanwhile, to reflect the significant bond-slip effect between concrete and reinforcement bars, the M-P stress-strain model is modified to account for the slippage by assuming the bar strain is the sum of the bar deformation and the slip, while the anchorage slip is theoretically derived and validated through benchmarking the pull-out tests. Additionally, a concrete layer between the precast concrete and the cast-in-situ concrete is incorporated to reflect the features of the interface. The proposed numerical modelling approach is validated through simulation of both interior and exterior precast beam-to-column connection tests. The validated models are subsequently employed to investigate the influences of key factors such as the compression-softening and the bond-slip effect on the analysis of the cyclic behavior of the precast beam-to-column connections. Results demonstrate that the proposed model is capable of reproducing the typical behavior of precast beam-to-column connections and can serve as an effective tool for the seismic performance analysis and investigation of design parameters of precast connections.

Keywords: finite element modelling, precast concrete, beam-to-column connection, cyclic behavior, softened damage-plasticity model, bond-slip effect, post-cast interface

1. Introduction

Precast concrete structures are widely used in industrial and residual buildings around the world including the United State, Japan, New Zealand and China, and they have various advantages compared with the traditional cast-in-situ concrete structures, including the product quality, construction speed, less manual labor, low environmental pollution, and so on [1]. Among different kinds of precast concrete structure systems at present, frame structures are particularly suitable for precast concrete industry since the beam and column components are very convenient for standardization, prefabrication and assembling. For example, in the past 5 years precast frame systems have been applied in more than 1 million m^2 buildings in China. In precast concrete frame structures, the beam-to-column connections are the crucial part as they affect not only the overall performance of the structures but also the cost and construction efficiency. Therefore, it is of great interest in studying the design methodologies, detailing, and analysis models of the precast concrete beam-to-column connections.

Most of the past investigations into the seismic performance of precast beam-to-column connections have been conducted using reversal cyclic loading tests on large size specimens, e.g., the work by Park and Bull [2], Alcocer et al. [3], Im et al. [4], Xue and Yang [5], Kulkarni and Li [6], Li and Kulkarni [7], Cai et al. [8], Chen et al. [9], Guan

*Corresponding author.
Email addresses: dcfeng@seu.edu.cn (De-Cheng Feng), g.wu@seu.edu.cn (Gang Wu), Yong.Lu@ed.ac.uk (Yong Lu)

et al. [1], etc. Through physical experiments, direct comparisons have been made between the various precast beam-to-column connections and their conventional monolithic counterparts in terms of the strength, ductility and energy dissipation capacities. However, experimental studies are usually costly and time consuming, and can be restricted by the test facilities and space [10]. Furthermore, the behavior of the beam-to-column connection is very complex and several parameters (e.g., axial load ratio, reinforcing details, concrete strength, etc.) have significant influences on its seismic performance; it is impractical to fully investigate all parameters through a limited number of experiments [11]. Therefore, numerical simulation has become a much needed means for the quantification of the influence of the underlying parameters, as well as further development of the design methodologies.

Generally, two kinds of numerical models are developed for precast beam-to-column connections. Models of the first kind are the macro-level joint models. These models [12, 13] usually use fiber elements to simulate the beams and columns, while additional rotational springs are introduced to the joint region to represent the bar slippage and the shear distortion of the joint panel, which are especially important for precast concrete structures due to the inevitable differences between the pre- and post-cast concrete. Yu and Tan [14] also proposed a new component-based joint model for precast concrete structures with an emphasis on the bond-slip behavior of longitudinal bars under large tension. Obviously, such a macro-level approach is simple and computationally efficient, thus is widely adopted for seismic analysis of precast beam-to-column connections. However, the calibration of the model parameters is usually difficult. Moreover, the macro-level joint models are suited mainly for analysis of whole or part of a frame structure, but cannot be used effectively for the investigation of the behavior within a joint or connection itself.

Models of the second kind are continuum-based finite element models, usually in a three-dimensional (3D) domain. These models are more elaborate and can provide detailed responses of the local region as compared with the macro models. Kulkarni et al. [15] and Li et al. [16] proposed a finite element model for precast hybrid-steel concrete connections under cyclic loading based on DIANA software, where two-dimensional (2D) plane stress elements were used for concrete and steel plates. The hysteretic curves of the connection were obtained and the influences of some critical design parameters were studied. Kaya and Arslan [17] used ANSYS to model post-tensioned precast beam-to-column connections under different stress levels; however, only monotonic behavior was obtained. Hawileh et al. [10] developed a detailed 3D finite element model for precast hybrid beam-to-column connections subjected to cyclic loads, and surface-to-surface contact between the beam and column faces were considered in the model. Bahrami et al. [18] numerically analyzed seismic performance of two new precast beam-to-column connections using ABAQUS software, covering the lateral resistance, ductility and energy dissipation of the connections. However, the analysis was also limited to monotonic loading.

It is fair to state that 3D finite element modelling represents the current trend in the numerical analysis of precast beam-to-column connections, due apparently to its presumed ability in describing the complex connection behavior in a realistic manner. However, there has been a lack of detailed discussion on the methodology and specific modelling techniques for precast beam-to-column connections, especially under reversal cyclic loading. This may be caused by the challenges in devising an adequate multi-axial concrete model with good computational stability under cyclic loading. Further, though widely realized of its significance, there has been a lack of efficient ways to represent the bar slippage (or bond-slip effect) in the critical regions, as well as the precast and cast-in-situ concrete interface, in a detailed FE model for the precast connections.

In light of the above-mentioned background, this paper aims at developing a rational procedure for the 3D finite element modelling of precast beam-to-column connections, with a particular emphasis on the cyclic behavior. A newly developed softened damage-plasticity model, which is numerically stable and reflects the typical cyclic behavior of reinforced concrete, is adopted for modelling of concrete. Meanwhile, to reflect the significant bond-slip effect between concrete and reinforcement bars at the joint core and plastic hinge regions of the precast connection assembly, the Menegotto-Pinto (M-P) stress-strain model is modified to account for the slip deformation. The modification to the M-P bar model is established on the basis of equivalent overall slip over the development length (anchorage slip) by adopting a modified bar strain to represent the sum of the bar deformation and the slip, while the anchorage slip is theoretically derived and validated through benchmarking the pull-out tests. An additional post-cast interface is set in the finite element modelling of the precast beam-to-column connections. The developed finite element model is validated through comparisons with the experimental results of several interior and exterior connections in terms of hysteretic load-displacement curves, stiffness degradation, energy dissipation, etc. Finally, the influences of the key factors, including the compression-softening, bond-slip effect, and the pre- and post-cast concrete interface on the cyclic performance of the precast beam-to-column connection are investigated.

2. Concrete damage-plasticity model with compression-softening

To model the typical cyclic behavior of the precast beam-to-column connections, a newly developed softened damage-plasticity model [19, 20] is adopted for concrete. This concrete model accounts for the compression-softening effect (Fig. 1) [21, 22] and is proven to be numerically robust for cyclic loading. The detailed derivation of the model can be seen in Refs. [19, 20]. Here it is briefly introduced.

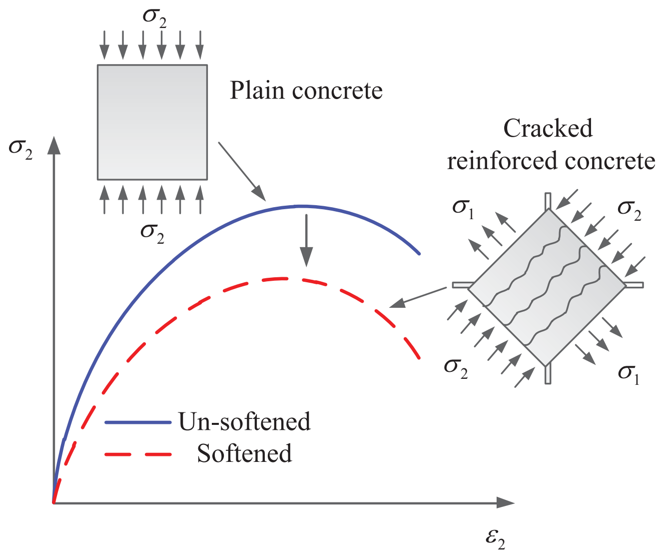

Figure 1: Compression-softening effect of reinforced concrete

Based on this model, the constitutive relation of concrete material is expressed as

$$\boldsymbol{\sigma} = (\mathbb{I} - \mathbb{D}^s) : \mathbb{E}_0 : (\boldsymbol{\epsilon} - \boldsymbol{\epsilon}^p) \tag{1}$$

where $\boldsymbol{\sigma}$ is the Cauchy stress tensor; $\mathbb{I}$ is the unit tensor; $\mathbb{E}_0$ is the fourth-order elastic modulus tensor; $\boldsymbol{\epsilon}$ is the total strain tensor; $\boldsymbol{\epsilon}^e$ and $\boldsymbol{\epsilon}^p$ are the elastic and plastic components of the strain tensor, respectively; $\mathbb{D}^s$ is the fourth-order damage tensor with compression-softening, which is given by

$$\begin{cases} \mathbb{D}^s = d^+\mathbb{P}^+ + d^{s-}\mathbb{P}^- \\ d^{s-} = 1 - \beta(1 - d^-) \end{cases} \tag{2}$$

in which $\mathbb{P}^+$ and $\mathbb{P}^-$ are the projection tensors; d^+ and d^- are the two damage variables representing the corresponding tensile and compressive behaviors of concrete; β is the softening coefficient.

The damage evolution is controlled by the energy release rates $Y^{\pm}$ [23, 24, 25], which be further simplified into energy equivalent strains $\overline{\epsilon}^{eq\pm}$ to represent the multi-dimensional damage evolution through uniaxial damage functions [26], i.e.,

$$\begin{cases} \overline{\epsilon}^{eq+} = \sqrt{\frac{2Y^+}{E_0}} \\ \overline{\epsilon}^{eq-} = \frac{1}{E_0(1-\alpha)}\sqrt{\frac{Y^-}{b_0}} \end{cases} \tag{3}$$

where E_0 is the initial elastic modulus; b_0 and α are the material parameters [23].

Consequently, the damage evolution functions can be determined by the uniaxial test data or some empirical functions. The following function proposed in [27, 28] is used herein

$$d^{\pm} = \begin{cases} 1 - \frac{\rho^{\pm} n^{\pm}}{n^{\pm}-1+(x^{\pm})^{n^{\pm}}} & x^{\pm} \leq 1 \\ 1 - \frac{\rho^{\pm}}{\alpha^{\pm}(x^{\pm}-1)^2+x^{\pm}} & x^{\pm} > 1 \end{cases} \tag{4}$$

in which

$$x^{\pm} = \frac{\overline{\epsilon}^{eq\pm}}{\epsilon_c^{\pm}}, \quad \rho^{\pm} = \frac{f_c^{\pm}}{E_0 \epsilon_c^{\pm}}, \quad n^{\pm} = \frac{1}{1-\rho^{\pm}} \tag{5}$$

where $f_c^{\pm}$ is the tensile/compressive peak strength; and $\epsilon_c^{\pm}$ is the strain corresponding to the peak strength in compression/tension; $\alpha^{\pm}$ is the tensile/compressive descending parameter that controls the shape of the descending part of the stress-strain curve.

The expression of softening coefficient β is derived based on the softened truss model (STM) [22], namely,

$$\beta = \frac{1}{\sqrt{1 + 400\overline{\epsilon}_{max}^{e+}}} \tag{6}$$

In addition, the plastic strain $\boldsymbol{\epsilon}^p$ can be determined through the empirical model developed by Faria et al. [29] and modified by Wu [30] is adopted, i.e.,

$$\dot{\boldsymbol{\epsilon}}^p = b^p \overline{\boldsymbol{\sigma}} \tag{7}$$

where b^p is the plastic flow parameter as

$$b^p = \xi^p E_0 H(\dot{d}^-) \frac{\langle \boldsymbol{\epsilon}^e : \dot{\boldsymbol{\epsilon}} \rangle}{\overline{\boldsymbol{\sigma}} : \overline{\boldsymbol{\sigma}}} \geq 0 \tag{8}$$

where ξ^p is the plastic coefficient. It should be noted that the tensile plastic strain is neglected since it is relatively small compared with the compressive one and has little influence of the entire structural behavior.

Moreover, to avoid mesh dependency issue when simulating softening responses [31, 32, 33, 34], the fracture energy is commonly employed for mesh regularization [35, 36, 37]. However, since the damage evolution function is rather complex, the material parameters cannot be explicitly expressed by the fracture energy. To simplify the procedure, we choose to select the appropriate descending parameters $\alpha^{\pm}$ in Eq. (4) to ensure constant energy dissipation under different mesh dimensions, in a similar way as adopted by Berto et al. [38], i.e.,

$$\frac{G_f^{\pm}}{l_{ch}} = \int \sigma^{\pm} d\epsilon^{\pm} \tag{9}$$

where $G_f^{\pm}$ are the tensile and compressive fracture energy, respectively; l_{ch} is the characteristic length related to the element dimension of the mesh

$$l_{ch} = \sqrt[m]{V_{ele}} \tag{10}$$

where V_{ele} is the volume of the element in the mesh; m is the dimension of the problem domain.

The standard tensile fracture energy of concrete can be found from the CEB 1990 model code. The compressive fracture energy, on the other hand, remains a subject of debate in structural engineering, especially for reinforced concrete. In this paper, the values recommended by Saritas and Filippou [36] are adopted.

3. Steel M-P model with bond-slip effect

3.1. Menegotto-Pinto model for reinforcement

The well-known Menegotto-Pinto (M-P) model, which accounts for the Bauschinger′s effect, is used for reinforcing steel bars, including both longitudinal and transverse bars. The model was first developed by Menegotto and Pinto [39], and then modified by Filippou et al. [40] to incorporate the isotropic hardening effect, and has proven to be good in reproducing the behavior of reinforcing steel bars. The skeleton curve of the model is actually a bilinear model, whose yield strength is f_y, and the elastic modulus is E_s, post-yield modulus is $E_h = bE_s$, in which b is the hardening ratio. The hysteretic behavior is defined by two sets of asymptote straight lines, as shown in Fig. 2. At the reversal point, the curve unloads with the initial elastic stiffness E_s, and then a curved transition is made by the two asymptote straight lines with slopes E_s and E_h, respectively. The monotonic curve of the stress-strain relation is

$$\sigma = \begin{cases} E_s \epsilon_s & \epsilon_s \leq \epsilon_y \\ f_y + E_h \left(\epsilon_s - \epsilon_y\right) & \epsilon_s > \epsilon_y \end{cases} \tag{11}$$

The hysteretic curve is given by

$$\sigma^* = b\epsilon^* + \frac{(1-b)\,\epsilon^*}{\left(1+\epsilon^{*R}\right)^{1/R}} \tag{12}$$

with

$$\epsilon^* = \frac{\epsilon - \epsilon_r}{\epsilon_0 - \epsilon_r}, \quad \sigma^* = \frac{\sigma - \sigma_r}{\sigma_0 - \sigma_r} \tag{13}$$

where $(\epsilon_0,\ \sigma_0)$ correspond to the strain and stress at the intersection point of the two asymptote straight lines; $(\epsilon_r,\ \sigma_r)$ correspond to the strain and stress at the last reversal point; R is the coefficient that controls the shape of the transition curve in order to better represent the Bauschinger′s effect. After each reversal, the point sets $(\epsilon_0,\ \sigma_0)$ and $(\epsilon_r,\ \sigma_r)$ are updated.

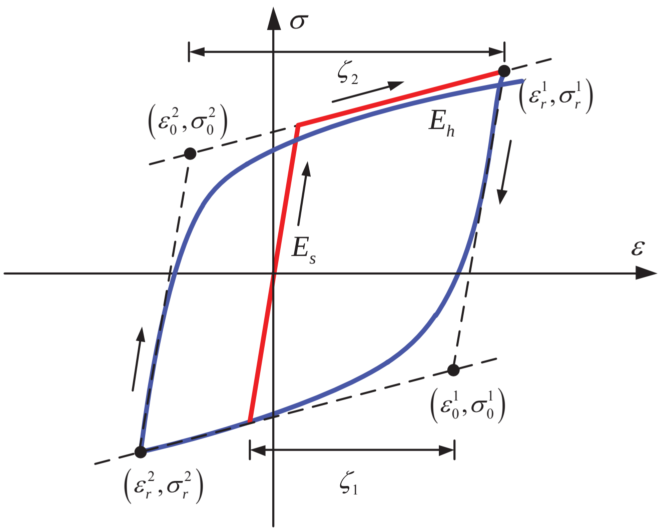

Figure 2: Menegotto-Pinto uniaxial stress-strain model

3.2. Analytical derivation of the bar slip

The bond-slip effect is an important factor that influences the behavior of the beam-to-column connections subjected to cyclic loadings. For precast concrete structures, this effect is even more significant since the quality of the post-cast concrete in the joint core region cannot be guaranteed as in the monolithic structures. The perfect bond assumption will lead to an over-estimate of the load capacity [41]. Therefore, the bond-slip effect should be carefully considered in the numerical model.

An explicit representation of the bond-slip mechanism may be achieved by incorporating contact or spring elements at the interface between the solid elements (representing concrete) and beam/truss elements (representing reinforcement) in a 3D finite element models, with the properties of the contact or spring element being assigned to simulate for example a tri-linear bond stress-slip relationship. Although such an approach is potentially more accurate, it requires a very complex pre-processing step for the pairing of the slave nodes from the beam/truss elements and the master nodes from the solid elements, and increases significantly the computational cost due to increased DOFs and elements.

In more recent years, another way of considering the bond-slip effect has emerged in numerical modelling for macro-level analysis of reinforced concrete responses [12, 14, 42] and fiber elements [43, 44, 45, 46, 47]. A bar stress-slip relation is derived by assuming the distribution of the bond stress, which represents the bond-slip spring, to formulate a component-based element. Likewise, the stress-stain relation of the reinforcement bars may be modified to incorporate the slip effect in the formulation of a fiber element. Although the method is indirect and may be less accurate, it provides an effective means to reconcile between the numerical accuracy and efficiency.

It should be noted, however, previous works [45, 46] along this line have mostly assumed a large enough anchorage length in the derivation, and consequently the applicability is restricted. Moreover, the approach has not been examined in a 3D finite element modelling environment. In the present study, we derive the slippage of different reinforcement bars (continuous or anchored) in the joint region with different anchorage lengths (enough or not) and different shapes (straight or bent). The result is used to modify the uniaxial M-P model to reflect bond-slip, which is then implemented conveniently in a 3D finite element analysis of beam-to-column connections. Details of the derivation are given in what follows.

A stepped bond stress distribution is assumed according to previous studies [48], as shown in Fig. 3. The bond stress for the elastic range ($\epsilon_s \leq \epsilon_y$) is $u_{be} = 1.0\sqrt{f_c'}$, while the bond stress for the inelastic range ($\epsilon_s > \epsilon_y$) is $u_{by} = 0.5\sqrt{f_c'}$ [14]. Based on the static equilibrium condition, the bar stress distribution can be derived with the bond stress definition, and the bar strain distribution is subsequently obtained. Finally, the total bar slippage s of the developed length L_d can be evaluated by integrating the strain field as

$$s = \int_0^{L_d} \epsilon(x)\, dx \tag{14}$$

and the full developed length L_d is given by

$$L_d = \underbrace{\frac{f_y d_b}{4u_{be}}}_{L_{ed}} + \underbrace{\frac{\left(f_u - f_y\right) d_b}{4u_{by}}}_{L_{yd}} \tag{15}$$

where L_{ed} is the full developed length for elastic part; L_{yd} is the full developed length for plastic part; d_b is the bar diameter; f_u is the ultimate fracture stress.

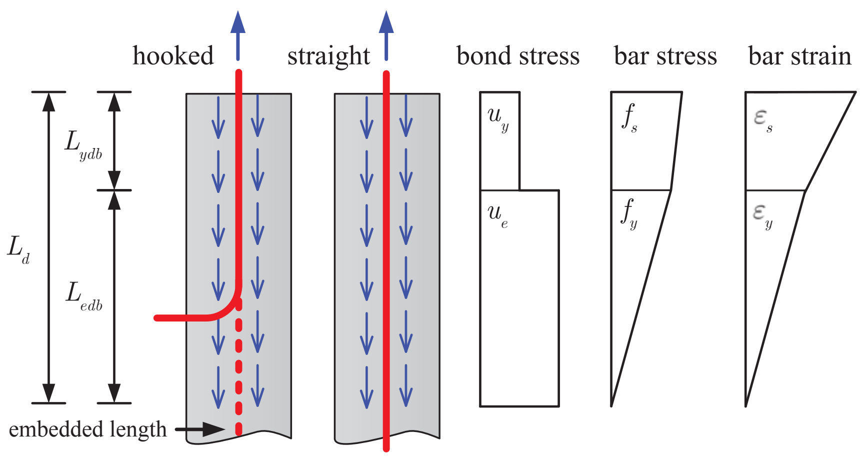

Figure 3: Bond-slip distribution at the beam-column joint interface

In a general situation, continuous and anchored bars are common used in the joint region, and the actual embedded length L_{embd} of the bar may not cover the full developed length L_d. Therefore, different scenarios should be considered to obtain the respective expressions of the bar slippage. For continuous bars, the opposite side of the joint core (which is actually under compression) is assumed to be the start point of the bond-slip distribution, and the slip at the start point is assumed to be zero, which means the embedded length is just the joint width and the plastic hinge length. For anchored bars, the embedded length is realistic one for straight anchored bars, or can be treated as a straight bar with an equivalent embedment length for bent bars [14]

$$L_{embd} = L_{embd}^{b} + 5d_b \tag{16}$$

where L_{embd}^{b} is the length of the embedded straight part of the bent bar.

According to the relation of the embedded length and the developed length of the bar, as shown in Fig. 4, the following scenarios can be formulated:

- Sufficient embedded length, $L_{embd} > L_d$, as shown in Fig. 4(a).

  (a) Fully elastic: if the applied strain (at the right end in the figure) is less than the yield strain ($\epsilon_s \leq \epsilon_y$), the developed elastic bond length L_{edb} can be determined by the force equilibrium

  $$L_{edb} = \frac{f_s d_b}{4u_{be}} \tag{17}$$

  Then the slip can be obtained by integrating the strain profile over the developed bond length

  $$s = \int_0^{L_{edb}} \epsilon(x)\, dx = \frac{\epsilon_s}{2} L_{edb} \tag{18}$$

  (b) Elastoplastic: if the applied strain is over the yield strain ($\epsilon_s > \epsilon_y$), the corresponding developed bond length L_{db} can be divided into two parts, an elastic part (L_{edb}) and a plastic part (L_{ydb}), i.e.,

  $$L_{db} = \underbrace{\frac{f_y d_b}{4u_{be}}}_{L_{edb}} + \underbrace{\frac{\left(f_s - f_y\right) d_b}{4u_{by}}}_{L_{ydb}} \tag{19}$$

  Thus the slip is

  $$s = \int_0^{L_{edb}} \epsilon(x)\, dx + \int_{L_{edb}}^{L_{ydb}} \epsilon(x)\, dx = \frac{\epsilon_y}{2} L_{edb} + \frac{\epsilon_y + \epsilon_s}{2} L_{ydb} \tag{20}$$

  Note that if the strain at the loaded end ϵ_s reaches the rupture strain ϵ_u, the bar will fail by a rupture mode.

- Insufficient total embedded length but sufficient elastic embedded length, $L_d > L_{embd} > L_{ed}$, as shown in Fig. 4(b).

  In this case, the first two developing stages of the slip are the same as Eqs. (18) and (20) in case (1) since the elastic embedded length is sufficient. However, when the bar stress at the loaded end is over the yield strength (hardening), the bar can be stressed through the start point (continuous bars) or the free-end (anchored bars), consequently the elastic and plastic developed bond lengths will be

  $$L_{ydb} = \frac{\left(f_s - f_y\right) d_b}{4u_{by}}, \quad L_{edb} = L_{embd} - L_{ydb} \tag{21}$$

  The strain profiles are different for continuous bars and anchored bars since the boundary conditions are totally different. For continuous bars, the slip at the start point is assumed to be zero, while for anchored bars the free-end slip s_0 may occur and the strain profile should be modified to the blue dashed line in Fig. 4(b) to ensure zero strain at the free-end. Thus, the total slip can be grouped into

– Continuous bar:

$$s_{cont} = \int_0^{L_{edb}} \epsilon(x)\,dx + \int_{L_{edb}}^{L_{ydb}} \epsilon(x)\,dx = \frac{\epsilon_{end} + \epsilon_y}{2} L_{edb} + \frac{\epsilon_y + \epsilon_s}{2} L_{ydb} \tag{22}$$

– Anchored bar:

$$s_{anch} = s_0 + \int_0^{L_{edb}} \epsilon(x)\,dx + \int_{L_{edb}}^{L_{ydb}} \epsilon(x)\,dx = s_0 + \frac{\epsilon_y}{2} L_{edb} + \frac{\epsilon_y + \epsilon_s}{2} L_{ydb} \tag{23}$$

For continuous bars, the strain ϵ_{end} at the start point is

$$\epsilon_{end} = \frac{L_{ed} - L_{edb}}{L_{ed}} \epsilon_y \tag{24}$$

For anchored bars, the free-end slip s_0 can be calculated according to the model by Alsiwat and Saatcioglu [49]

$$s_0 = s_1 \left(\frac{u_e}{u_u}\right)^{2.5} \tag{25}$$

with

$$s_1 = \left(\frac{30}{f_c'}\right)^{0.5}, \quad u_e = \frac{f_{se} d_b}{4 L_{edb}}, \quad u_u = \left(20 - \frac{d_b}{4}\right)\left(\frac{f_c'}{30}\right)^{0.5} \tag{26}$$

where s_1 is the ultimate slip at the free-end; u_e is the elastic bond stress at the free-end; u_u is the ultimate bond stress; f_{se} is the maximum bar stress ($\le f_y$) in the elastic developed bond length. Note that if u_e reaches u_u ($s_0 \ge s_1$), the bar will fail by a pull-out mode.

- Insufficient total length and insufficient elastic embedded length, $L_{embd} < L_{ed}$, as shown in Fig. 4(c).

  If the embedded length is shorter than the required full elastic developed length, at first it is still the same as Eq. (18), then the bar will be stressed over the entire length. If the applied strain is still in the elastic stage, The developed elastic bond length is actually the full embedded length, i.e., $L_{edb} = L_{embd}$. Similarly, the slip can be derived according to bar type, i.e.,

  – Continuous bar:

$$s_{cont} = \int_0^{L_{embd}} \epsilon(x)\,dx = \frac{\epsilon_{end} + \epsilon_s}{2} L_{embd} \tag{27}$$

  – Anchored bar:

$$s_{anch} = s_0 + \int_0^{L_{embd}} \epsilon(x)\,dx = s_0 + \frac{\epsilon_s}{2} L_{embd} \tag{28}$$

  in which the start point strain for continuous bars will be

$$\epsilon_{end} = \frac{L_{ed} - L_{embd}}{L_{ed}} \epsilon_s \tag{29}$$

  Pull-out failure will occur if $s_0 \ge s_1$. If this does not happen when the bar yields at the loaded end, then the slip is the same as Eq. (22) or (23).

In summary, the slip for the three cases can be expressed as:

- Case 1: $L_{embd} > L_d$

$$s = \begin{cases} \frac{\epsilon_s}{2} L_{edb} & \epsilon_s \le \epsilon_y \quad L_{edb} = \frac{f_s d_b}{4 u_{be}} \\ \frac{\epsilon_y}{2} L_{edb} + \frac{\epsilon_y + \epsilon_s}{2} L_{ydb} & \epsilon_s > \epsilon_y \quad L_{edb} = L_{ed},\ L_{ydb} = \frac{(f_s - f_y) d_b}{4 u_{by}} \end{cases} \tag{30}$$

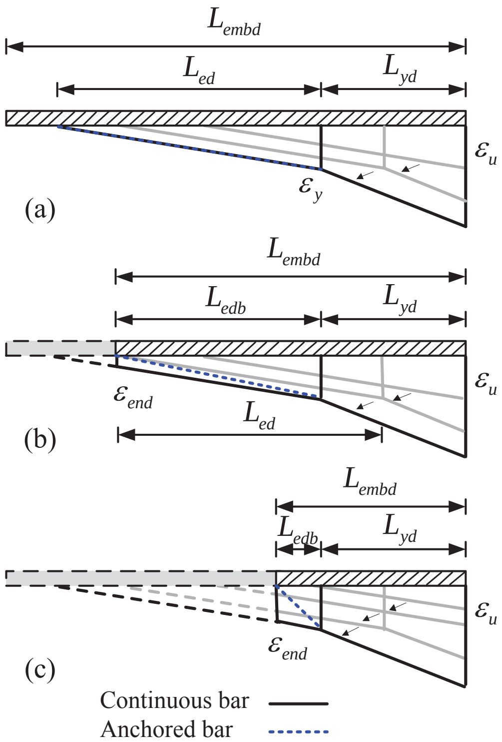

Figure 4: Strain profiles of different bar embedded length

- Case 2: $L_d > L_{embd} > L_{ed}$

$$s = \begin{cases} \frac{\epsilon_s}{2} L_{edb} & \epsilon_s \le \epsilon_y \quad L_{edb} = \frac{f_s d_b}{4u_{be}} \\ \frac{\epsilon_y}{2} L_{edb} + \frac{\epsilon_y + \epsilon_s}{2} L_{ydb} & \epsilon_s > \epsilon_y \quad L_{edb} = L_{ed},\ L_{ydb} = \frac{(f_s - f_y) d_b}{4u_{by}} \le L_{embd} - L_{ed} \\ s_{cont}\ in\ Eq.\ (22)\ or\ s_{anch}\ in\ Eq.\ (23) & \epsilon_s > \epsilon_y \quad L_{ydb} = \frac{(f_s - f_y) d_b}{4u_{by}},\ L_{edb} = L_{embd} - L_{ydb} \end{cases} \tag{31}$$

- Case 3: $L_{embd} < L_{ed}$

$$s = \begin{cases} \frac{\epsilon_s}{2} L_{edb} & \epsilon_s \le \epsilon_y \quad L_{edb} = \frac{f_s d_b}{4u_{be}} \le L_{embd} \\ s_{cont}\ in\ Eq.\ (27)\ or\ s_{anch}\ in\ Eq.\ (28) & \epsilon_s \le \epsilon_y \quad L_{edb} = L_{embd} \\ s_{cont}\ in\ Eq.\ (22)\ or\ s_{anch}\ in\ Eq.\ (23) & \epsilon_s > \epsilon_y \quad L_{ydb} = \frac{(f_s - f_y) d_b}{4u_{by}},\ L_{edb} = L_{embd} - L_{ydb} \end{cases} \tag{32}$$

The bar stress-slip relationship can be determined according to the above Eqs. (30)-(32) for different bar embedded length situations. Note that two different failure modes may take place, namely bar rupture failure ($\epsilon_s \ge \epsilon_u$) and pull-out failure ($s_0 \ge s_1$), and whichever is reached it would be treated as the failure of the bar.

In order to validate the above proposed bar stress-slip model, several pull-out tests reported in [50] are simulated. Fig. 5 shows the comparison between the analytical and experimental results. A good agreement is observed, demonstrating the accuracy of the proposed model.

3.3. Modified uniaxial stress-strain relationship for reinforcement

For a precast beam-to-column column connection, the bar deformation in the joint and in the plastic hinge region includes two distinctive contributions: the bar deformation itself and the anchorage slip. The anchorage slip is associated with the bond-slip effect, and as mentioned before this effect may be accounted for by using an equivalent bar

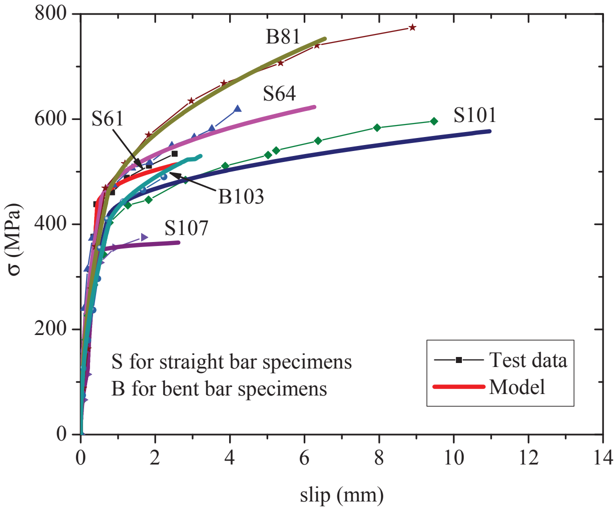

Figure 5: Validation of the proposed slip model by pullout tests

stress-strain relation model [46, 51]. In the 3D finite element model herein, the equivalent bar stress-strain relation is obtained based on the slip model described in Section 3.2. By uniformly distributing the slip into the bars at the joint core and plastic hinge region, the equivalent bar strain is obtained as

$$\epsilon_s' = \epsilon_s + \frac{s}{L_e} \tag{33}$$

where ϵ_s' is the modified bar strain accounting for slip; ϵ_s is the original bar strain; s is the total bar slip; L_e is the length of the bar at the joint core and plastic hinge.

Therefore, a modified M-P model can be developed for the bars in the joint core and plastic hinge with Eq. (33). The modifications are actually a reduction of the elastic stiffness and an elongation of the hardening branch for tension. In this present model a zero slip is assumed for bar under compression [46], thus the compressive curve of the M-P model remains unchanged.

The modifications are all illustrated in Fig. 6. In the monotonic skeleton for tension, the bar stress of the elastic stage can be written as

$$f_s = E_s\epsilon_s = E_s'\epsilon_s' \tag{34}$$

where E_s' is the modified elastic modulus accounting for bond-slip, and can be derived by substituting Eq. (33) into Eq. (34), i.e.,

$$E_s' = \frac{E_s\epsilon_s}{\epsilon_s'} = \frac{E_s}{1 + s/\left(\epsilon_s L_e\right)} \tag{35}$$

In the hardening stage, the following equilibrium should be satisfied

$$f_s = f_y + E_h\left(\epsilon_s - \epsilon_y\right) = f_y + E_h'\left(\epsilon_s' - \epsilon_y'\right) \tag{36}$$

Thus the modified hardening stiffness E_h' can be expressed by

$$E_h' = E_h\frac{\epsilon_s - \epsilon_y}{\epsilon_s' - \epsilon_y'} = \frac{E_h}{1 + \left(s - s_y\right)/\left(\epsilon_s L_e - \epsilon_y L_e\right)} = \frac{bE_s}{1 + \left(s - s_y\right)/\left(\epsilon_s L_e - \epsilon_y L_e\right)} \tag{37}$$

where s_y is the slip corresponding to the yield strain.

Finally, the tension monotonic curve considering bond-slip can be unified as

$$\sigma = \begin{cases} E'_s \epsilon'_s & \epsilon'_s \leq \epsilon'_y \\ f_y + E'_h \left(\epsilon'_s - \epsilon'_y\right) & \epsilon'_s > \epsilon'_y \end{cases} \tag{38}$$

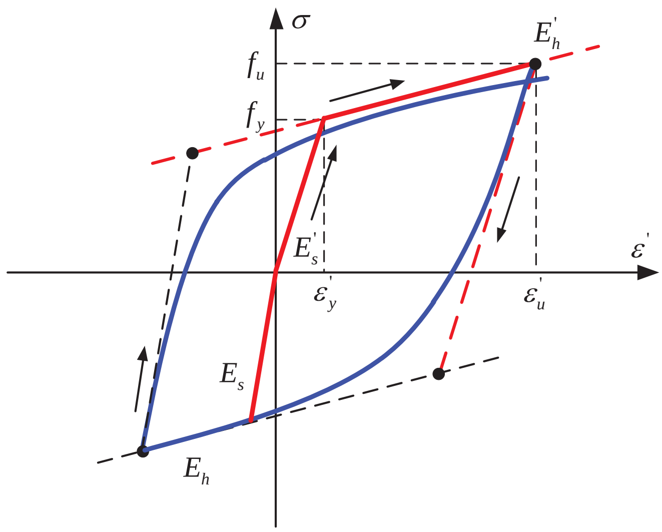

Figure 6: Modified stress-strain relation considering bond-slip for reinforcement bars

The hysteretic behavior is still defined by two asymptote straight lines, but the stiffness of the lines should be changed according to Eq. 38 [51]. The tensile unloading follows the initial stiffnessE'_s, and the transition is determined by asymptote lines with stiffness E'_s and E'_h (marked in red in Fig. 6, respectively. The compressive unloading and transition are the same as the original M-P model.

With the above modified stress-strain model for the reinforcing bars, the bond-slip effects in the joint core and plastic hinge region can be well represented without the need for an explicit bar-concrete interface treatment. Changing the constitutive models for reinforcement bars (both continuous ones and anchored ones) according to different embedded lengths can effectively represent the significant bond-slip effects in these regions. Therefore by applying a combination of the original and the modified M-P models, it is possible to simulate a variety of precast beam-to-column connections with a 3D finite element model in a computationally efficient way.

It should be noted that, the above approach is actually an implicit and macro-level way to consider bond-slip, thus the cyclic effects on the bond-slip responses are neglected, and the effects of bond deterioration on accumulation of strains in some cracks (strain localization) versus uniformly distributed cracks cannot be captured. The method aims at finding an effective means to reconcile between the numerical accuracy and efficiency. More elaborated approach to represent the bond-slip effect requires further work.

4. Finite element modelling strategy for precast beam-to-column connection

The above-mentioned material models are both implemented into the ABAQUS software through user-defined subroutine UMAT, thus 3D finite element model of precast beam-to-column connections can be developed with the incorporation of the above described material models using the ABAQUS software, and the implicit Newton-Raphson method is employed in the numerical calculations. Fig. 7 presents an overall view of a typical finite element model. The precast concrete beams and columns, as well as the post-cast concrete, are modelled with 8-node solid elements, while the reinforcement bars are modelled with 2-node truss elements. The reinforcement bars are embedded in concrete, which means the bar is fully bonded to the surrounding concrete. A 10 *mm* thick layer is arranged between the precast beam-column components and the post-cast concrete to represent the properties of the post-cast concrete at the interface, since it is another typical feature of precast concrete structures. The softened damage-plasticity model is used to model the concrete. The concrete strength for the post-cast interface is taken as $0.9f_c'$ to reflect the weakened material at the interface between the precast concrete and post-cast concrete. The modified M-P model is used for the bars inside the joint core and the beam/column plastic hinge region to account for the bond-slip effect, while the original M-P model is used for the reinforcement in the remaining regions. The plastic hinge length is computed by $L_e = L_{core} + 0.5h_{sec}$ [14], where L_{core} is the core width and h_{sec} is the hight of the section.

The mesh size is set as $50 \times 50 \times 50$ mm, correspondingly, the characteristic length is computed by Eq. (10). The tensile fracture energies are ranging from 100 N/m to 130 N/m, while the compressive fracture energies are ranging from 25000 N/m to 35000 N/m [36, 52]. With l_{ch} and $G_f^{\pm}$, the material descending parameters $\alpha^{\pm}$ can be easily determined through uniaxial tension and compression tests and Eq. (4).

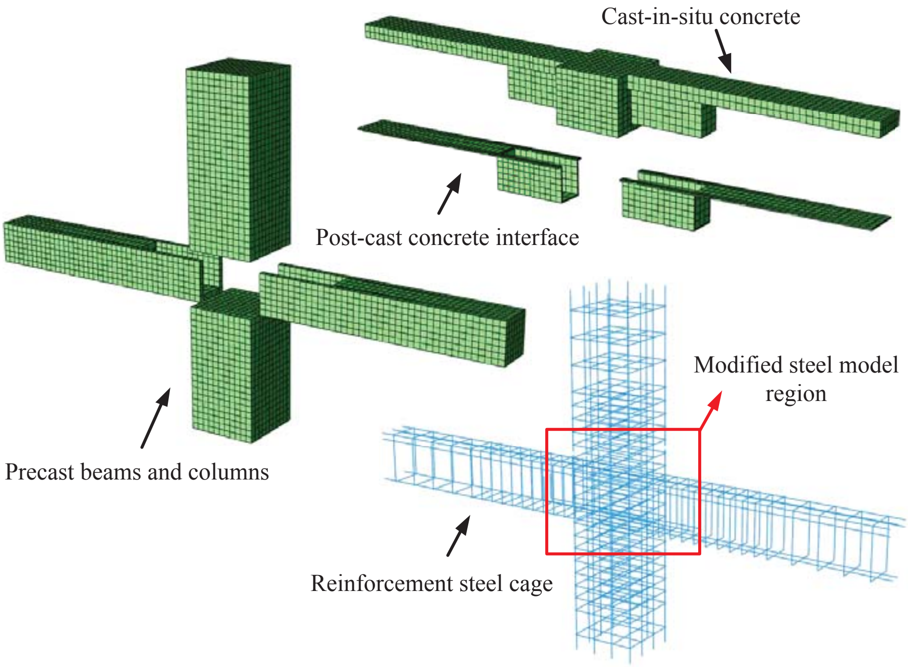

Figure 7: Finite element model for the precast beam-to-column connection

5. Model validations

To validate the finite element modelling strategy proposed in this paper, a series of precast interior and exterior beam-to-column connections is analyzed. The selected specimens have different failure patterns, thus the capability of the proposed method can be fully demonstrated.

5.1. Interior beam-to-column connections with flexure failure

Firstly two interior beam-to-column connections (specimen S2 and S3) tested by Guan et al. [1], which were characterized as flexure failure, were modelled. The schematic design of the connection is shown in Fig. 8, and the material properties of the concrete and reinforcement bars used in the specimens are listed in Table 1. Other details about the specimen information and experimental setup can be found in Ref. [1]. In analysis, the loading scheme is divided into two parts, i.e., first the axial load is applied on the top of the column through force control, then the lateral cyclic load is imposed at the same position via displacement control.

The numerical results for the flexure failure specimens S2 and S3 are demonstrated in Fig. 9, which shows a comparison of the computed load-displacement hysteretic curves (moment vs. drift angle) for S2 and S3, respectively,

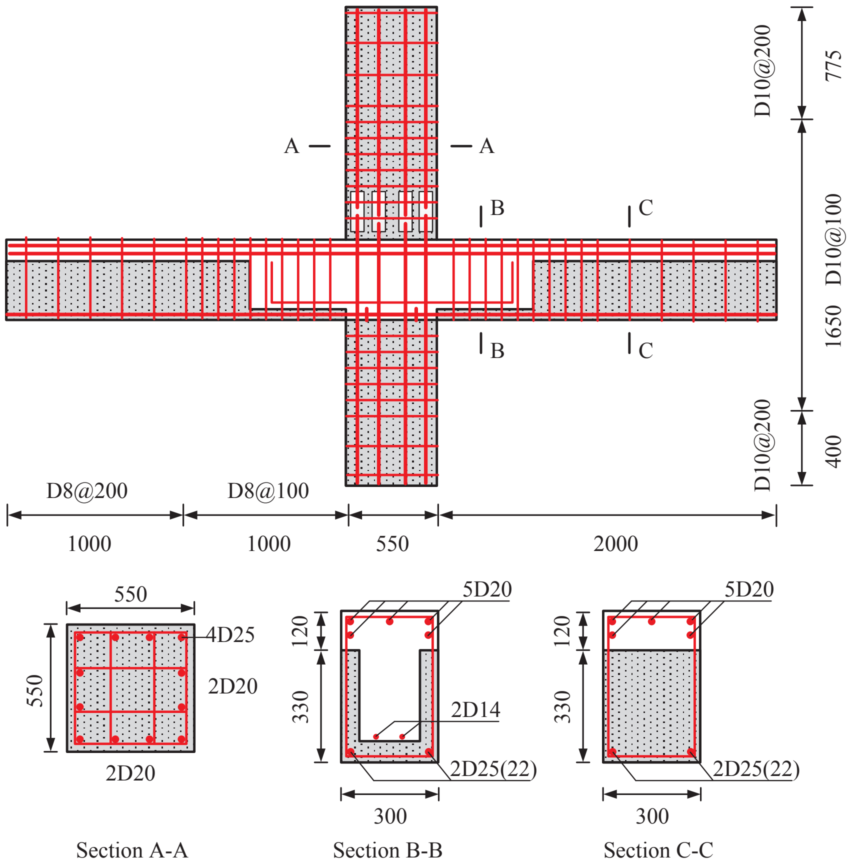

Figure 8: Schematic design of the flexure failure specimens S2/S3 by Guan et al. [1] (dimensions are in mm)

Table 1: Material properties of the interior beam-to-column connection specimens S2/S3

Concrete properties					
Concrete type	Precast columns		Precast beams		Connection zone
Compressive strength f'_c (MPa)	55.5		51.4		56.1
Reinforcement properties					
Bar diameter (mm)	D8	D10	D20	D22	D25
Area (mm^2)	50.2	78.5	314.0	379.9	490.6
Elasticity E_s (MPa)	2×10^5	2×10^5	2×10^5	2×10^5	2×10^5
Yield strength f_y (MPa)	448	433	448	450	429
Yield strain ϵ_y	0.00224	0.00216	0.00224	0.00225	0.00214
Ultimate strength f_u (MPa)	646	598	617	624	607
Hardening ratio b	0.01	0.01	0.01	0.01	0.01

with the test results. Good agreements can be observed. Actually the low-cycle fatigue is not considered in the material models, so only the first cycle (totally three in the experiments) of each drift angle applied to the specimens is used for comparison. The strength and stiffness of the connections for most cycles are predicted very well by the numerical models. Relatively speaking, the pinching effect appears to be less predicted by the numerical model. This is probably because of the fact that multiple (three) cycles were performed at each level of the displacement in the actual experiment, causing low-cycle fatigue, whereas in the numerical simulation such an effect has not been considered in the material models. Meanwhile, the concrete damaged plasticity (CDP) model in ABAQUS is also used to model the specimen S2, and the results are compared with that by the proposed model in Fig. 9(a). Obviously, the response predicted by the CDP is a little larger than the experimental results, and the pinching effect is also over-estimated. This may just because the compression-softening effect under tension-compression stress state is neglected in CDP, thus the shear behavior cannot be accurately represented.

In addition, the quantitative features of the hysteretic responses, i.e., stiffness degradation and energy dissipation, are also displayed in Fig. 10. The stiffness degradation is calculated according to the secant stiffness, which is defined as the slope of the secant line connecting the peak response points in positive and negative directions of each drift angle cycle. As can be seen, the degradation of stiffness from the numerical simulation matches well with the experimental counterpart. The initial stiffness of the specimens are slightly overestimated by the numerical models, this may be caused by the fact that the boundary conditions of the specimens cannot be accurately modelled in the simulation, since some DOFs of the supports are not restrained perfectly in the experiments. The experimental curves increased slightly in the drift angle range of 0.2-1% due to some friction between the supporting plates and rotating plate of the column base, which cannot be reflected in the model. A good agreement is also observed of the energy dissipation in the two specimens between the computed and test results.

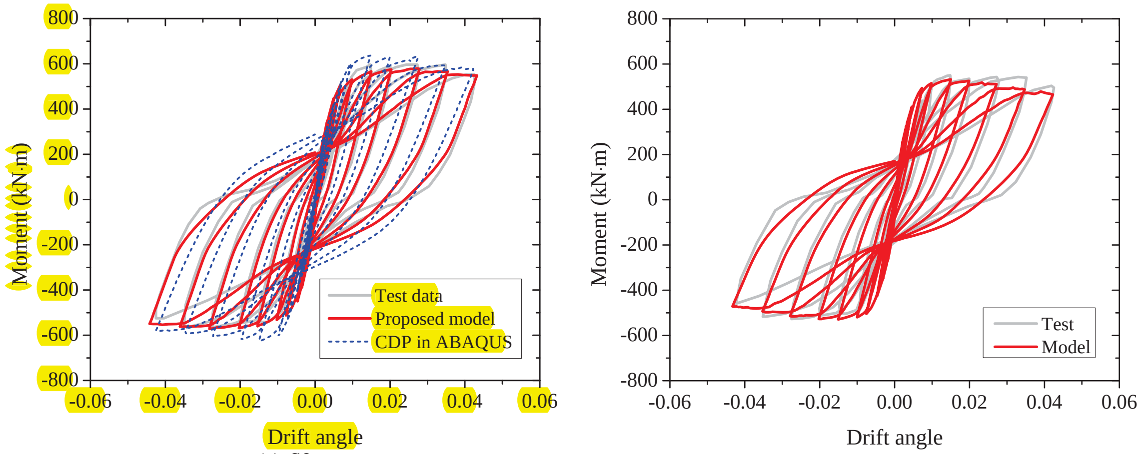

(a) S2 (b) S3

Figure 9: Load-displacement hysteretic curves of S2 and S3

Furthermore, Fig. 11 compares the failure modes of the specimens obtained from the numerical models and the experiments. The contour in the numerical models actually indicates the damage distribution of the specimens. For both specimen S2 and S3, the cracks formed at the beam ends and then gradually spread along the beam, and finally the specimens failed due to concrete crushing at the beam ends, i.e., a flexure type failure. These features are all well captured by the numerical models.

As a proof of the mesh convergence, the results of two different mesh sizes for S2, i.e., $50 \times 50 \times 50$ *mm* and $25 \times 25 \times 25$ *mm*, are also compared in Fig. 12, where both the hyseteretic responses for models with and without regularization are shown. It can be seen that the results by two different meshes show an obvious mesh-dependency if the regularization is not adopted, while the results are nearly the same after the regularization is used. This indicates that the regularization method adopted by this paper to avoid mesh-sensitivity issue is effective.

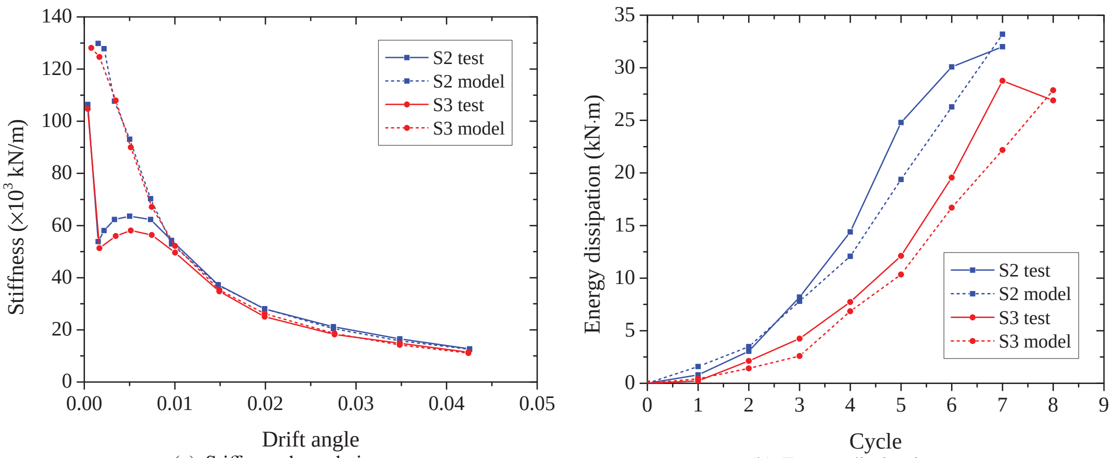

(a) Stiffness degradation (b) Energy dissipation

Figure 10: Quantitative features of the hysteretic curves of S2 and S3

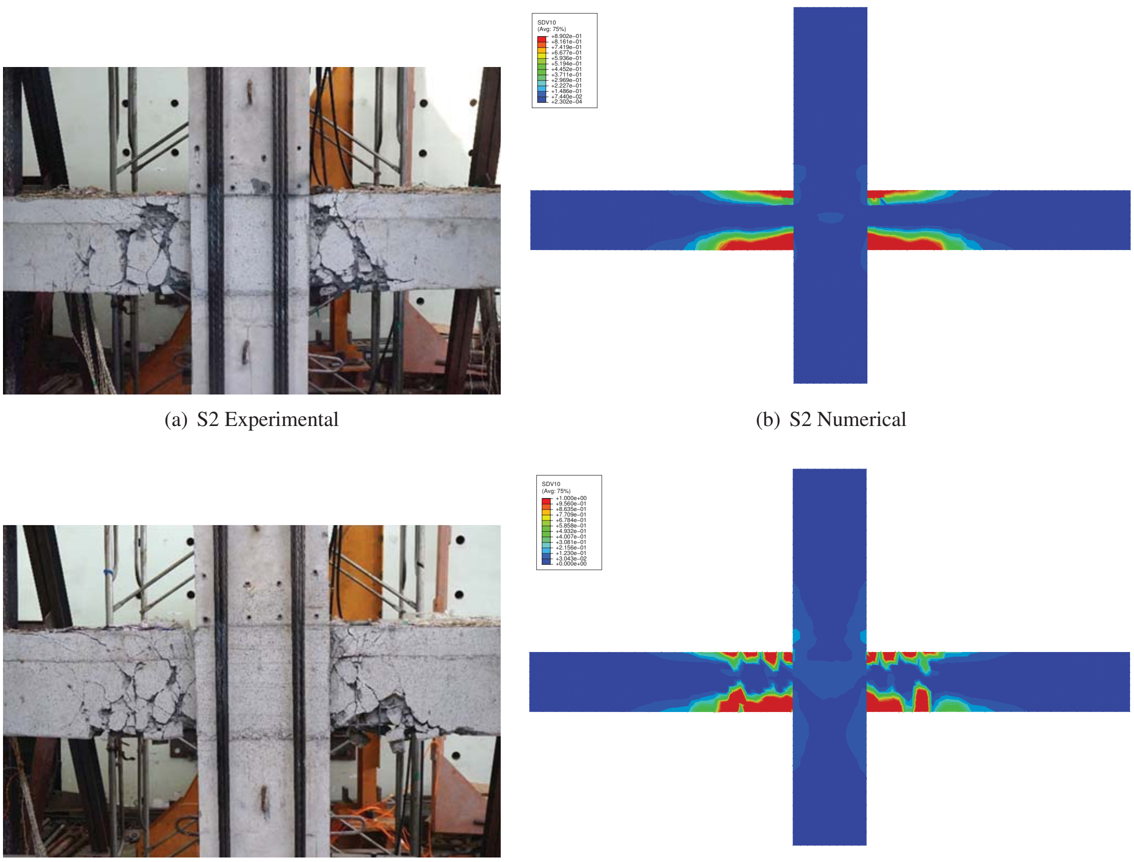

(a) S2 Experimental (b) S2 Numerical

(c) S3 Experimental (d) S3 Numerical

Figure 11: Experimental and numerical failure modes of S2 and S3

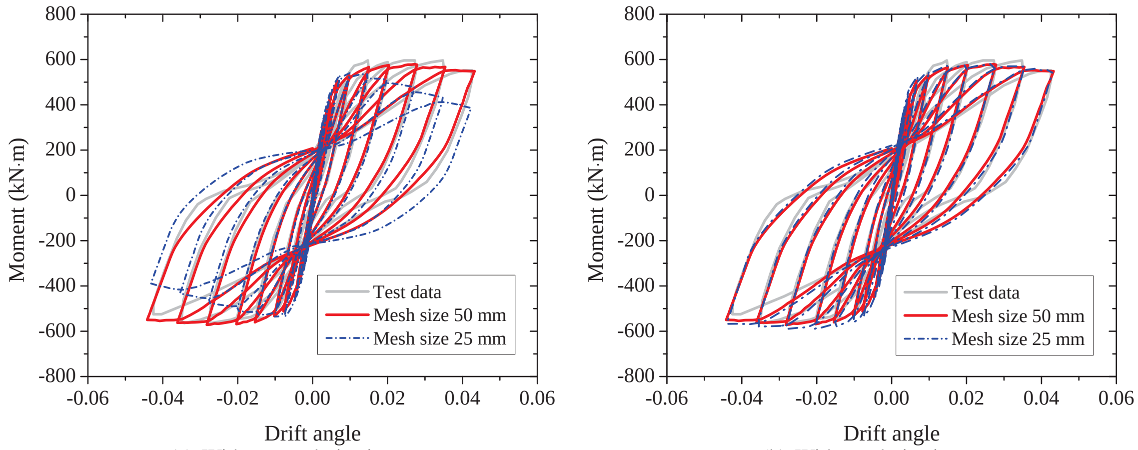

(a) Without regularization (b) With regularization

Figure 12: Results by different mesh size types for S2

5.2. *Interior beam-to-column connections with bond/shear failure*

Secondly two specimens (specimen SP3 and SP4) tested by Im et al. [4], which were characterized as bond/shear failure at the joint region, were analyzed. The specimens details, i.e., design and geometric information, are given in Fig. 13. The only difference between the two specimens are the longitudinal reinforcing ratios. Material properties for the specimens are listed in Table 2. The loading scheme in analysis is the same as the previous example.

Table 2: Material properties of the interior beam-to-column connection specimens SP3/SP4

Concrete properties					
Concrete type	Precast columns		Precast beams		Connection zone
Compressive strength f_c' (MPa)	47.5		35.1		34.9
Reinforcement properties					
Bar diameter (mm)	D13	D16	D25	D32	D35
Area (mm^2)	127	199	507	794	957
Elasticity E_s (MPa)	2×10^5	2×10^5	2×10^5	2×10^5	2×10^5
Yield strength f_y (MPa)	503	434	463	468	493
Yield strain ϵ_y	0.00251	0.00217	0.00231	0.00234	0.00246
Ultimate strength f_u (MPa)	583	585	630	599	605
Hardening ratio b	0.01	0.01	0.01	0.01	0.01

The numerical results for the bond/shear failure specimens SP3 and SP4 are displayed in Fig. 14, where the experimental and numerical cyclic responses of the specimens are compared. Evidently, the two responses match with each other quite well. The capacity, loading/unloading stiffness, residual deformation, as well as the energy dissipation, are all well reproduced by the numerical model. The measured load-carrying capacity for specimens SP3 and SP4 are 667.8 kN and 926.8 kN, respectively, while the predicted ones are 645.8 kN and 897.9 kN, respectively. The maximum error is only 3.2%. Especially, the pinching effect of the specimens is rather severer than the flexure failure specimens S2/S3, since obvious diagonal shear cracks were observed in the joint panel region, and significant bond-slip behavior was occurred in the joint due to the crushing of the beam end concrete. Due to the consideration of the compression-softening effect and bond-slip at the critical region in the proposed method, pinching effect caused by these features can be captured.

Fig. 15 further gives the experimental and numerical failure modes of the specimens, where the numerical failure modes are represented by the damage contours. Obviously, the X-shaped diagonal cracks at the joint panel are

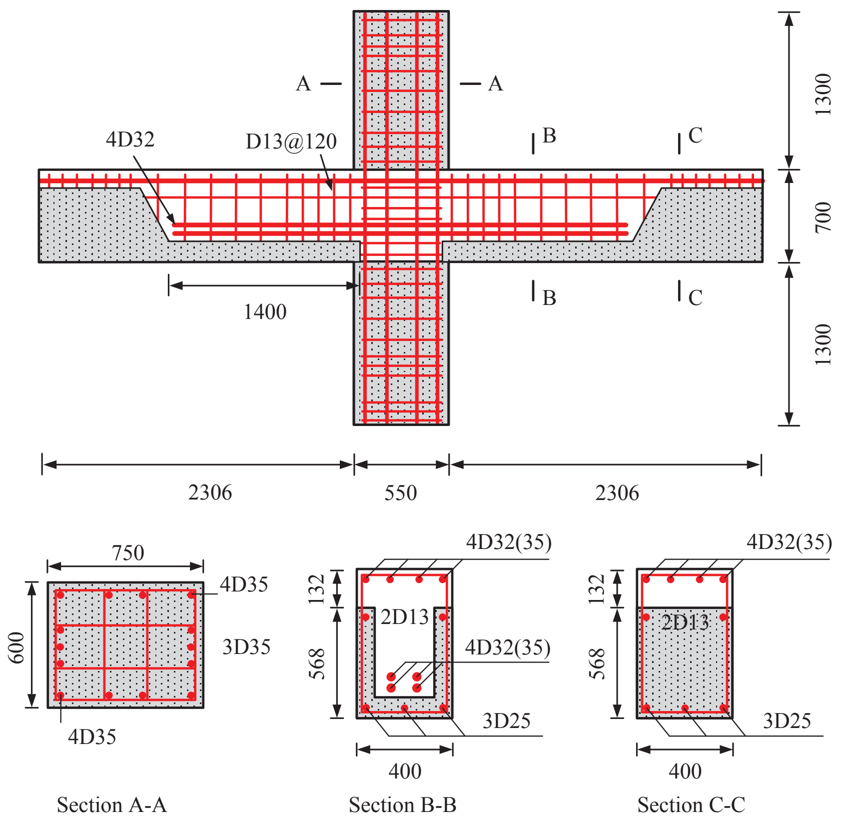

Figure 13: Schematic design of the bond/shear failure specimens SP3/SP4 by Im et al. [4] (dimensions are in mm)

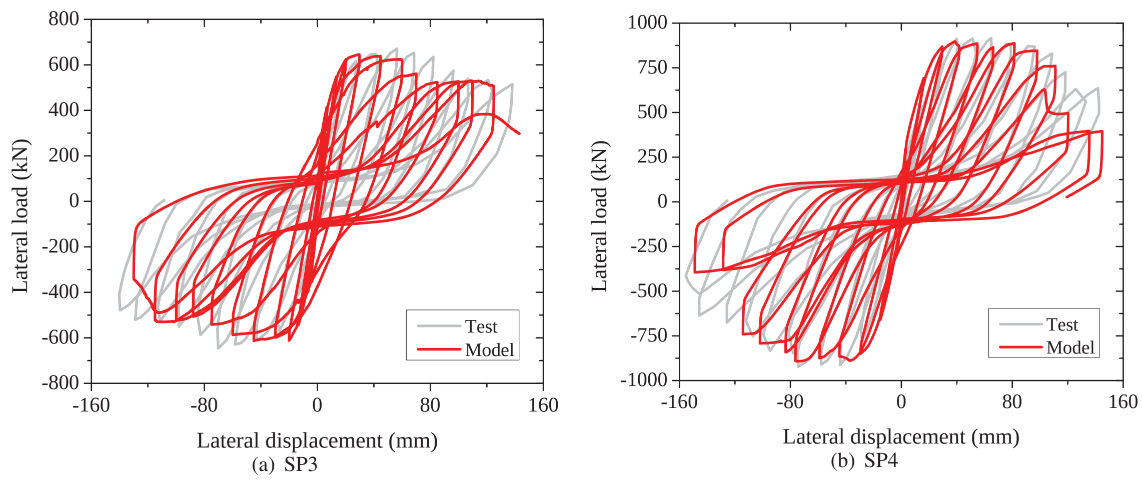

Figure 14: Load-displacement hysteretic curves of SP3 and SP4

predicted with highly satisfactory, and the distributed cracks and concrete crushing regions at the beam ends are also reflected very well.

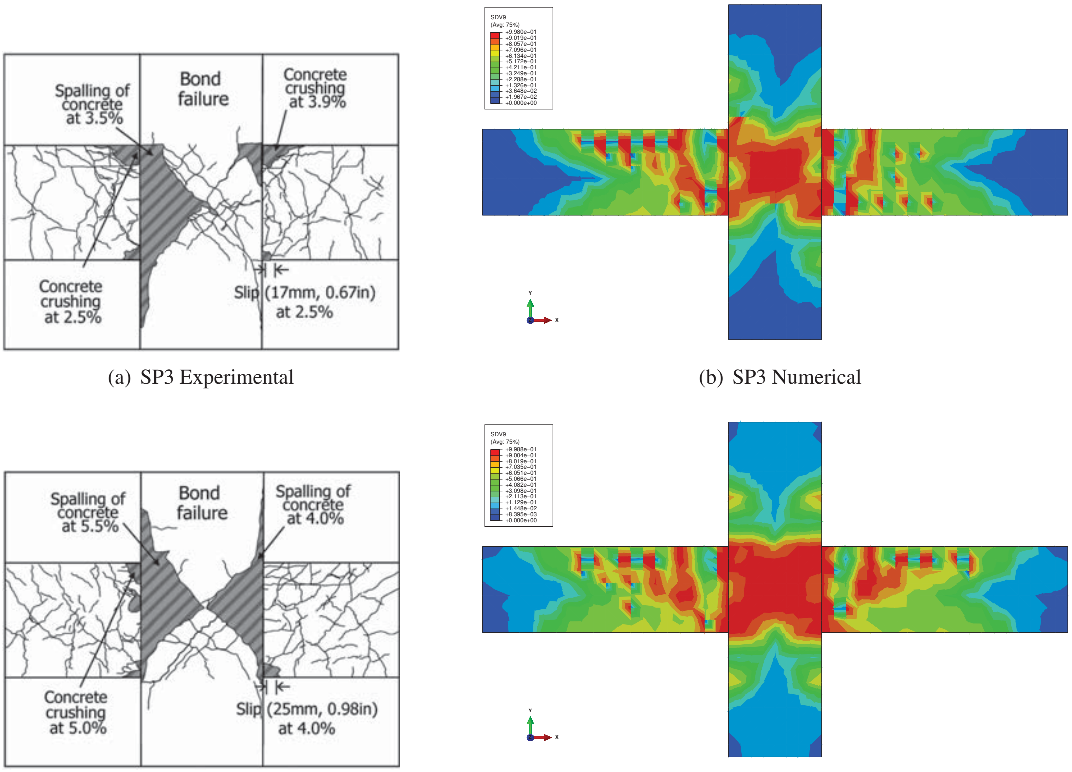

(a) SP3 Experimental (b) SP3 Numerical

(c) SP4 Experimental (d) SP4 Numerical

Figure 15: Experimental and numerical failure modes of SP3 and SP4

5.3. *Exterior beam-to-column connections with flexure failure*

Finally, two exterior beam-to-column connections with flexure failure were simulated. The connections were tested by Parastesh et al. [53] and specimens BCT3 and BCT4 were selected. The specimen design is shown in Fig. 16. The only changing variable is the spacing of the beam stirrups, i.e., it is 100 mm for BCT3 while 75 mm for BCT4. Material properties are given in Table 3. Note that some of the reinforcement properties were nor provided by the original research, such that they were determined by previous computational experience.

The numerical lateral load-displacement curves are shown in Fig. 17. Once again, the calculated results demonstrate highly accurate correlations to the experimental results. The hysteretic behavior of the specimens does not show any pinching effects since diagonal reinforcement bars were used in the joint core, which will prevent the diagonal shear cracks in this region. Fig. 18 displays the computed damage distribution versus the observed failure mode of the specimens. As can be seen, plastic hinge was occurred at the beam ends, which agrees with the experimental results well. The damage extent of specimen BCT3 is greater than BCT4 since the spacing of the beam stirrups of BCT3 is smaller than that of BCT4. Meanwhile, the damage of the upper side of the beam is greater than the lower side for both specimens, since lap-splicing of the longitudinal reinforcement is used in the connection zone.

6. Investigation of influences of modelling approaches

The proposed finite element model for the precast beam-to-column connections has been shown to be effective and capable of reproducing typical cyclic behavior of the connections with different failure types. Understandably, the

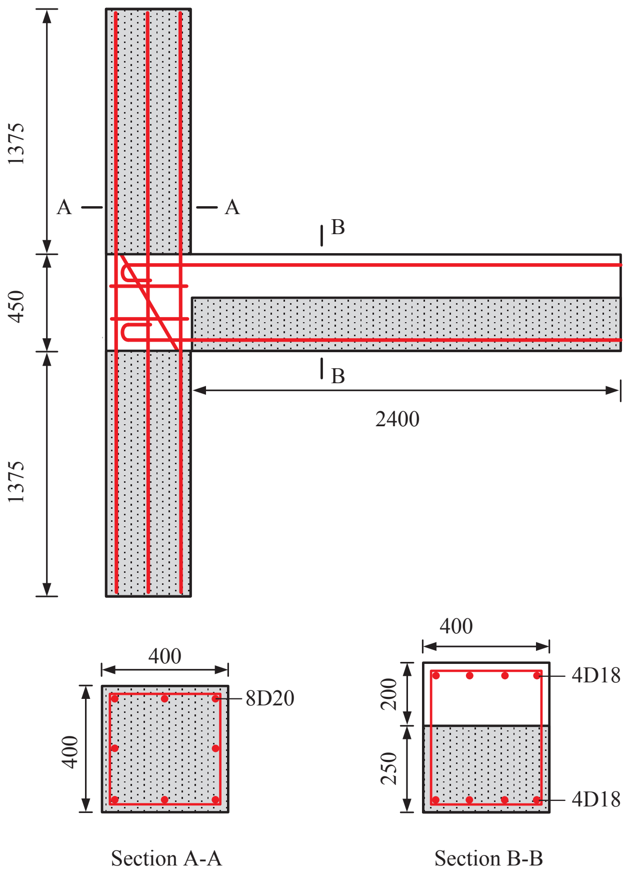

Figure 16: Schematic design of the exterior specimens BCT3/BCT4 by Parastesh et al. [53] (dimensions are in mm)

Table 3: Material properties of the exterior beam-to-column connection specimens BCT3/BCT4

Concrete properties			
Concrete type	Precast		Grout
Compressive strength f'_c (MPa)	27		25
Reinforcement properties			
Bar diameter (mm)	D10	D18	D20
Area (mm^2)	78.5	254.3	314
Elasticity E_s (MPa)	2×10^5	2×10^5	2×10^5
Yield strength f_y (MPa)	300	400	400
Yield strain ϵ_y	0.0015	0.002	0.002
Hardening ratio b	0.01	0.01	0.01

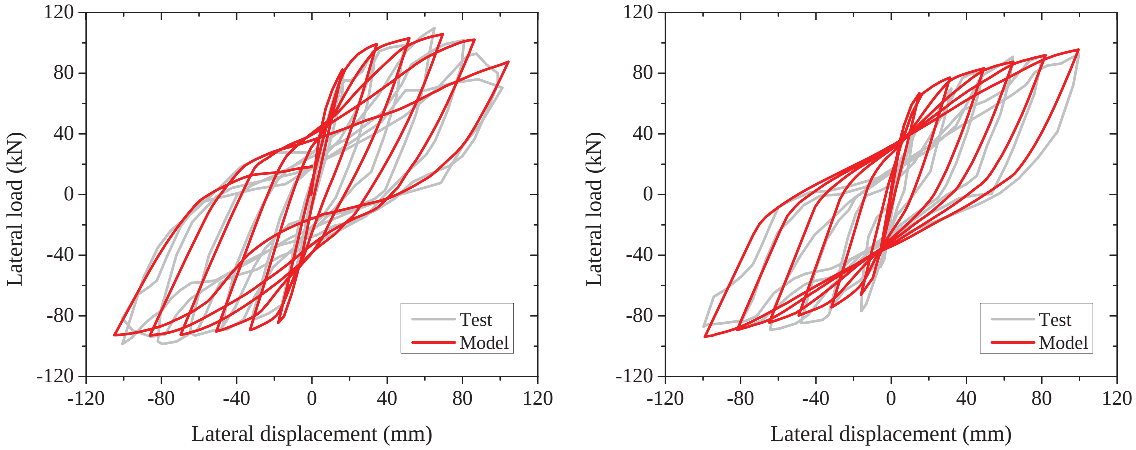

(a) BCT3 (b) BCT4

Figure 17: Load-displacement hysteretic curves of BCT4 and BCT4

cyclic behavior of the connections is influenced by the damage accumulation in the concrete material and the bond-slip effect, and likewise the performance of the finite element model will be affected by how these factors are represented in the modelling framework. In this section, some key influencing factors, namely the compression-softening effect, bond-slip effect and property of the post-cast concrete interface, are studied based on the validated finite element models in previous section. It should be noted that only one specimen in each of the previous simulated groups is investigated to save space, and the interior connection S2 with flexure failure, interior connection SP3 with bond/shear failure and exterior connection BCT3 with flexure failure are chosen.

6.1. Influence of compression-softening effect

As mentioned before, the compression-softening effect is a typical behavior of reinforced concrete under a multi-dimensional stress state, especially when subjected to shear. The presence of transverse cracks will cause the compressive strength softening in the orthogonal direction, thus it is important to be considered in the numerical simulation of reinforced concrete structures; otherwise the load capacity of the structure may be over-estimated. Fig. 19 demonstrates the hysteretic load-displcement curves of the selected specimens obtained by the models without and with compression-softening, where ”C-S” denotes compression-softening. As can be observed clearly, in general, the responses predicted by the model without compression-softening are markedly stiffer than that predicted by the model with compression-softening, especially after yielding. The peak strengths for the specimen S2 by the two models (with and without C-S) are 579 kNm and 648 kNm, respectively, and for SP3 they are 645.8 kNm and 796.2 kNm, respectively, while for BCT3 they are 105.7 kNm and 127.8 kNm, respectively. Evidently, for the specimen SP3 with significant shear behavior, the extent of over-estimation will be higher since shear behavior indicates tesion-compression stress state and compression-softening is just corresponds to this stress state.

6.2. Influence of bond-slip effect

Bond-slip effect is another key factor that should be accounted for in cyclic analysis of the precast concrete beam-to-column connections. This effect is particularly significant in the joint and plastic hinge regions, and more so for the precast beam-column connections. This is because in these regions the reinforcing bars tend to undergo large bond-slip actions (for example the reinforcing bars in the beams tend to be pulled on one side of the joint and pushed on the other side). Moreover, the reversal cyclic loadings will cause several cracks in the regions, which intensifies the deterioration of bond between concrete and reinforcement bars. For precast connections, the quality of the precast concrete in the joint region cannot be fully guaranteed, therefore the bond-slip problem becomes even more important.

The numerical results with and without accounting for the bond-slip effect are compared in Fig. 20. The response by the model without bond-slip (perfect bond assumption) appears to show gross overestimate of the overall strength,

(a) BCT3 Experimental

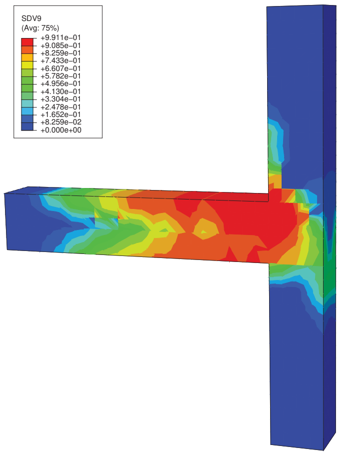

(b) BCT3 Numerical

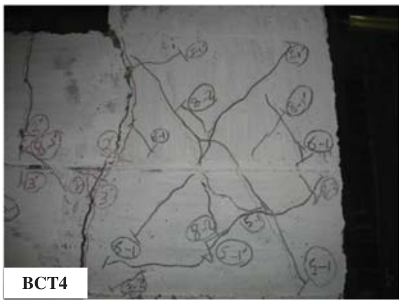

(c) BCT4 Experimental

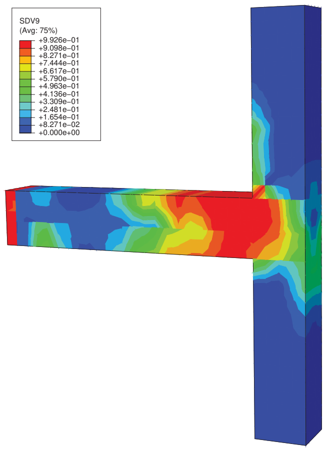

(d) BCT4 Numerical

Figure 18: Experimental and numerical failure modes of BCT3 and BCT4

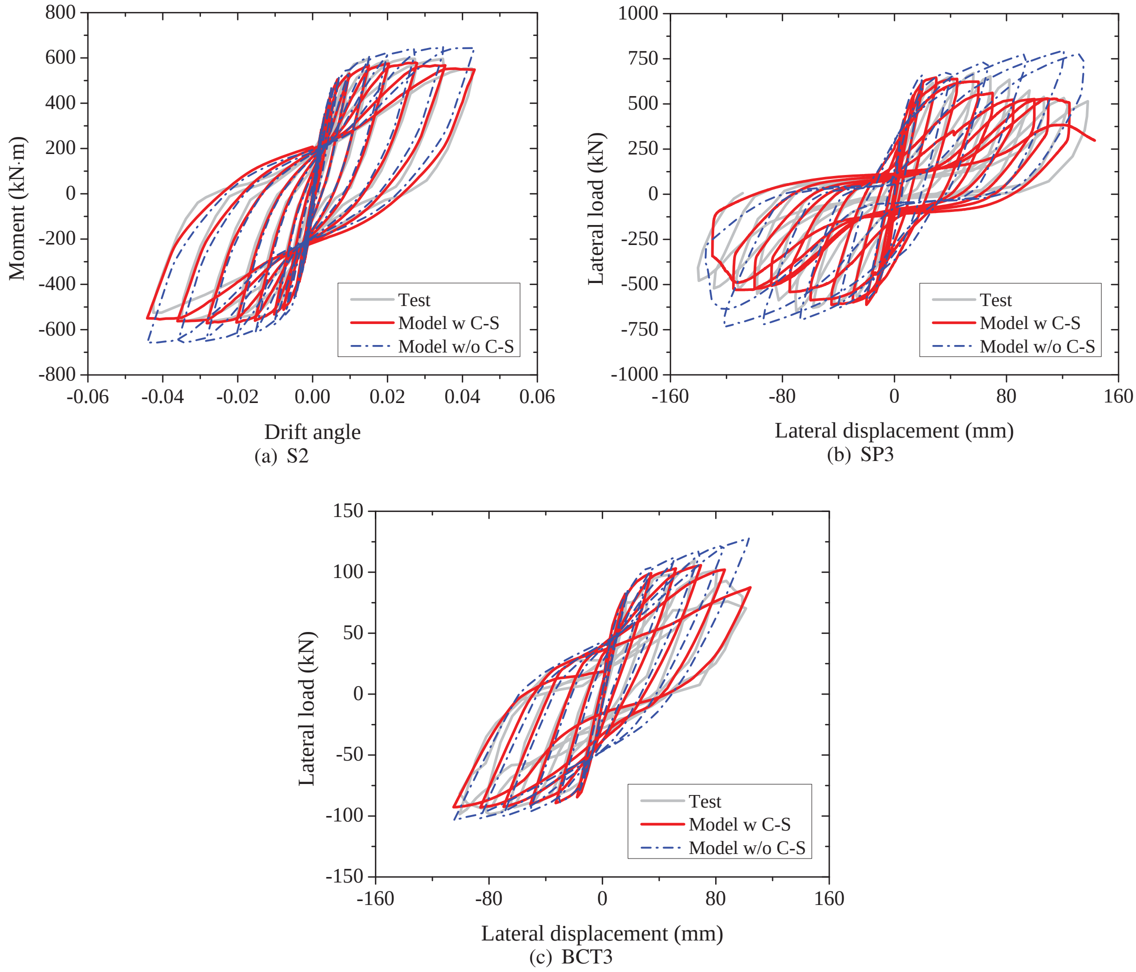

Figure 19: Results by models with and without compression-softening

energy dissipation, as well as the stiffness. All of these indicate the inadequacy of ignoring the bond-slip effect in the analysis of the cyclic behavior of beam-to-column connections.

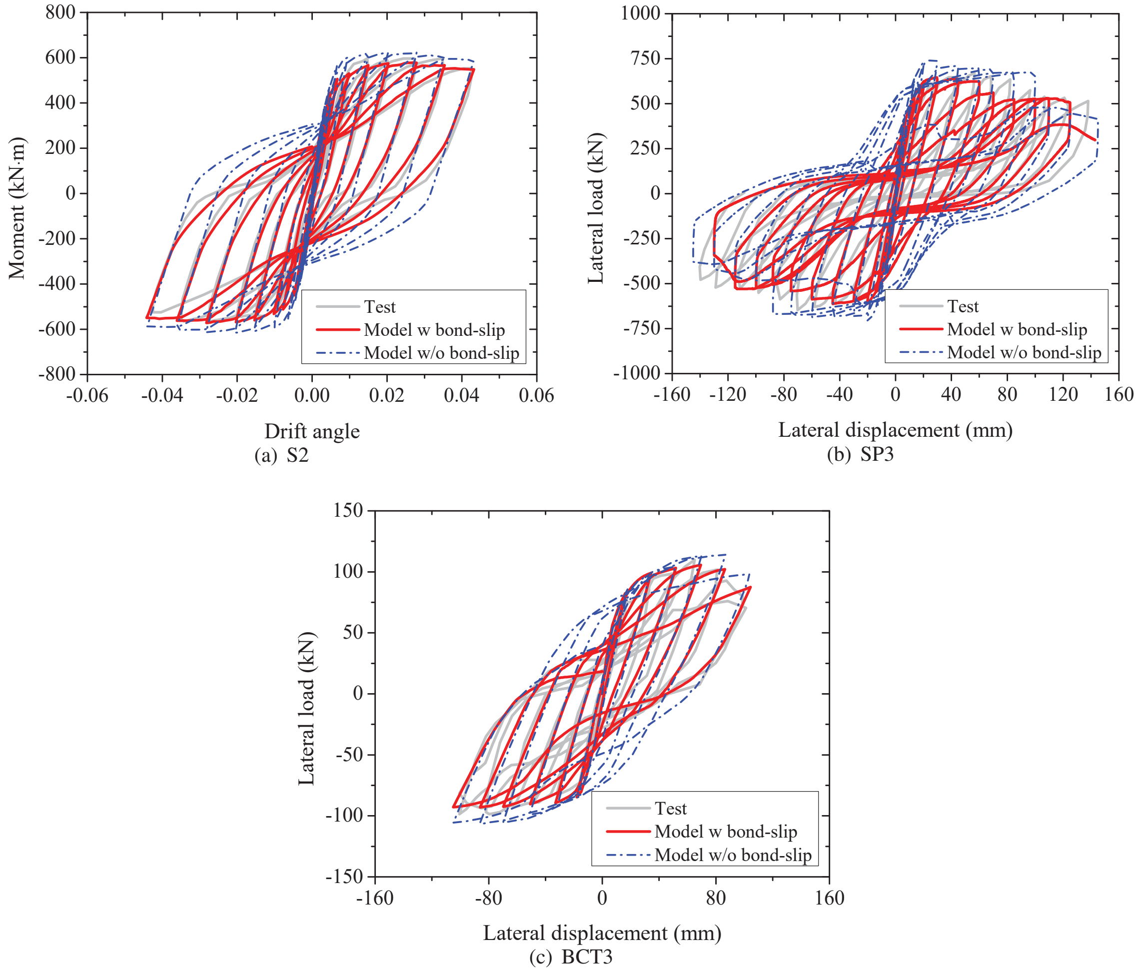

Figure 20: Results by models with and without bond-slip

6.3. Influence of post-cast concrete interface

In previous studies on finite element analysis of precast beam-to-column connections, the interface between the precast beam and column components and the post-cast concrete is usually neglected. That is to say, the modelling of the precast structure is actually the same as that of the monolithic structure. However, it is widely recognized that the interface between the precast components and the post-cast concrete is the weak part of the structure, although some methods are adopted to improve the integrality of the structure, e.g., making rough of the concrete faces or adding extra reinforcement bars.

To taking into account the interface effect, in this paper a 10 *mm* thick layer is arranged to model this interface and the properties of concrete is set as 90% of the post-cast concrete, i.e., both the compressive and tensile strengths are set as 90% of their original counterparts. Here the influence of different properties of the interface layer is also investigated. Three levels of concrete material properties are assigned to the interface, namely, 0.8, 0.9, and 1.0 times of the original strength. The results are shown in Fig. 21. It can be observed from the figure that the overall strength and stiffness of the connection are enhanced with the increase of the concrete property of the post-cast concrete interface. With respect to the experimental results, a reduction of the concrete property to 90% of the original property is deemed to be appropriate for the type of precast connections under consideration. 0.9 f_c' matches the experimental results very well, while if monolithic behavior is assumed ($1.0f_c'$), the behavior of the precast connection will be over-estimated. Fig. 22 also demonstrates the damage contour of the interface layer for specimen S2 as an example. The damaged part will spread with the decrease of the concrete property.

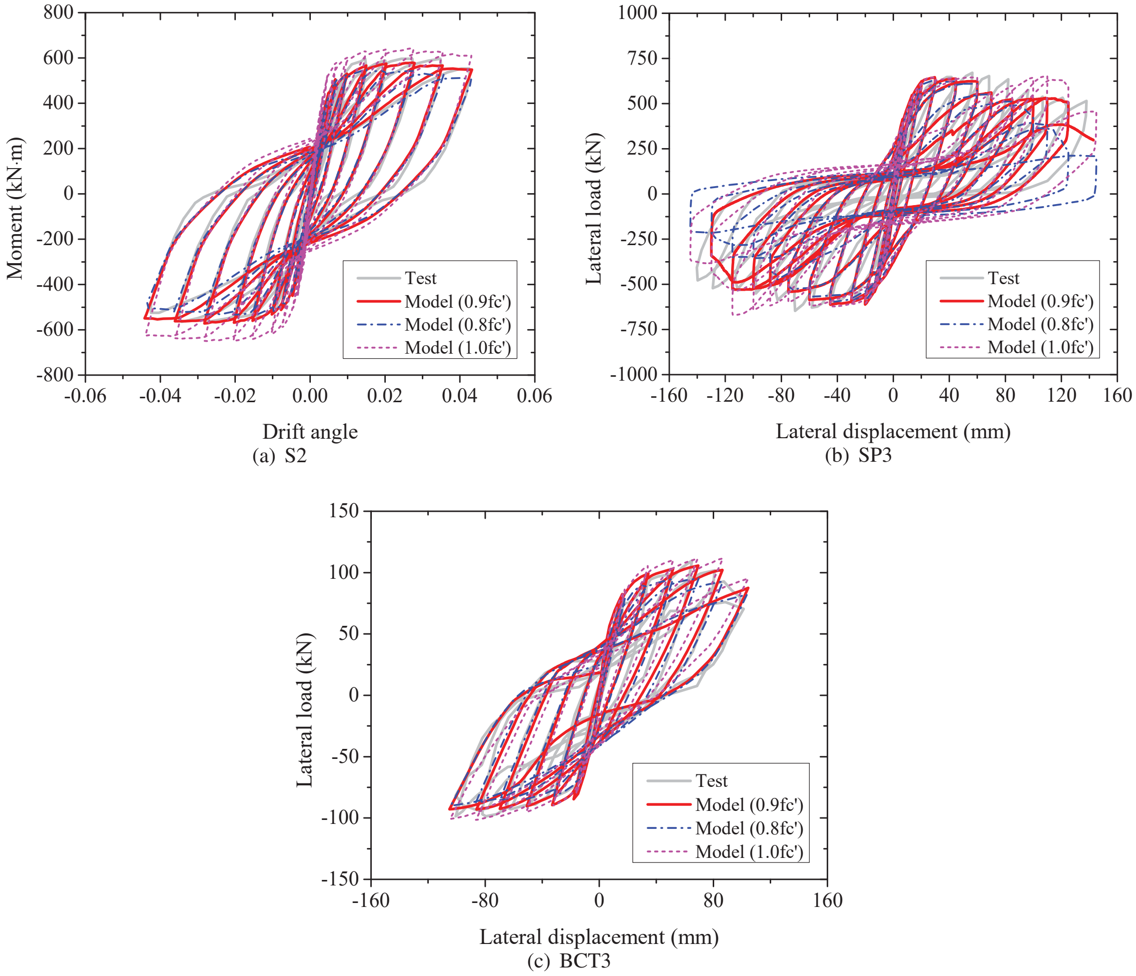

Figure 21: Results by models with different interface properties

7. Conclusions

The paper presents a 3D finite element analysis procedure for precast concrete beam-to-column connections subject to reversal cyclic loading. Important considerations to deal with the cyclic loading include the use of a softened damage-plasticity model for concrete, and the modification of the M-P model for reinforcement bars in critical bond and anchorage regions. Furthermore, the concrete interface between the precast beam and column components and the post-cast concrete are also accounted for in the model.

The modified M-P model for reinforcing bars is established on the basis of an equivalent overall slip inside the joint core and plastic hinge region. The overall anchorage slip of the bar is theoretically derived and validated through benchmarking with pull-out tests, and from there the M-P model is modified by defining an equivalent strain to encompass both the actual bar strain and the slip. Although an indirect method, this treatment is effective in handling the bond-slip effect, and it is particularly suitable in the 3D numerical modelling of precast beam-to-column connections.

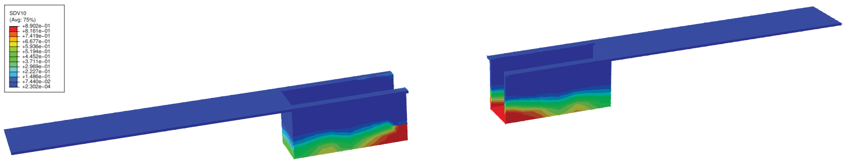

(a) $1.0f_c'$

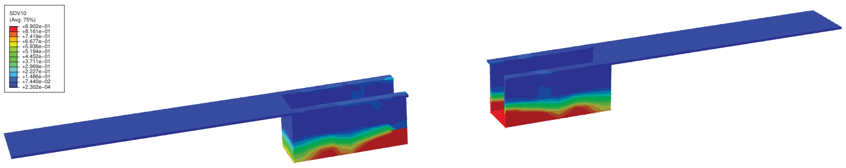

(b) $0.9f_c'$

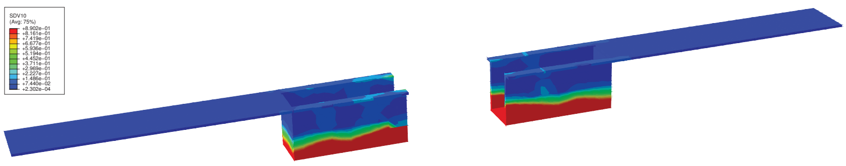

(c) $0.8f_c'$

Figure 22: Damage of the interface layer for specimen S2

The proposed numerical model is used to simulate a set of representative precast beam-to-column connections with different failure modes. The results indicate that the numerical model can capture the typical cyclic behavior, failure mode, stiffness degradation and energy dissipation of the connection. With the numerical model, the influence of key factors on the cyclic behavior of the precast connections and their modelling, namely the compression-softening effect, the bond-slip effect and the properties of the post-cast interface, are also studied. In general, the developed numerical modelling scheme provides an effective and efficient way to modelling the cyclic behavior of precast beam-to-column connections with good accuracy. The modelling approach can be used to investigate the influences of the design parameters on the seismic behavior of precast beam-to-column connections, reducing the need for costly and time-consuming experimental work.

Acknowledgements

Financial supports from the National Natural Science Foundation of China (Grant No. 51708106), the Natural Science Foundation of Jiangsu Province (Grant No. BK20170680), and the Fundamental Research Funds for the Central Universities are greatly appreciated. The first author Dr. De-Cheng Feng also want to thank his beloved wife Ms. Xiao-Jing Song for supporting his work over the past decades and giving birth to their dearest baby at 07-07-2018.

References

[1] D. Guan, C. Jiang, Z. Guo, H. Ge, Development and seismic behavior of precast concrete beam-to-column connections, Journal of Earthquake Engineering (2016) 1–23.

[2] D. Bull, R. Park, Seismic resistance of frames incorporating precast prestressed concrete beam shells, PCI JOURNAL 31 (4) (1986) 54–93.

[3] S. M. Alcocer, R. Carranza, D. Perez-Navarrete, R. Martinez, Seismic tests of beam-to-column connections in a precast concrete frame, PCI journal 47 (3) (2002) 70–89.

[4] H. Im, H. Park, T. Eom, Cyclic loading test for reinforced-concrete-emulated beam-column connection of precast concrete moment frame, ACI Structural Journal 110 (1) (2013) 115.

[5] W. Xue, X. Yang, Seismic tests of precast concrete, moment-resisting frames and connections., PCI journal 55 (3).

[6] S. A. Kulkarni, B. Li, Seismic behavior of reinforced concrete interior wide-beam column joints, Journal of Earthquake Engineering 13 (1) (2008) 80–99.

[7] B. Li, S. A. Kulkarni, Seismic behavior of reinforced concrete exterior wide beam-column joints, Journal of Structural Engineering 136 (1) (2009) 26–36.

[8] J. Cai, H. Zhu, J. Feng, Y. Liu, L. Huang, Experimental study on seismic behavior of middle joints of scope system, Journal of Central South University: Science and Technology 43 (5) (2012) 1894–1901.

[9] S. Chen, W. Yan, J. Gao, Experimental investigation on the seismic performance of large-scale interior beam-column joints with composite slab, Advances in Structural Engineering 15 (7) (2012) 1227–1237.

[10] R. Hawileh, A. Rahman, H. Tabatabai, Nonlinear finite element analysis and modeling of a precast hybrid beam–column connection subjected to cyclic loads, Applied Mathematical Modelling 34 (9) (2010) 2562–2583.

[11] C. Roehm, S. Sasmal, B. Novák, R. Karusala, Numerical simulation for seismic performance evaluation of fibre reinforced concrete beam–column sub-assemblages, Engineering Structures 91 (2015) 182–196.

[12] L. N. Lowes, N. Mitra, A. Altoontash, A beam-column joint model for simulating the earthquake response of reinforced concrete frames, Pacific Earthquake Engineering Research Center, College of Engineering, University of California Berkeley, 2003.

[13] O. C. Celik, B. R. Ellingwood, Modeling beam-column joints in fragility assessment of gravity load designed reinforced concrete frames, Journal of Earthquake Engineering 12 (3) (2008) 357–381.

[14] J. Yu, K. H. Tan, Numerical analysis with joint model on rc assemblages subjected to progressive collapse, Magazine of Concrete Research 66 (23) (2014) 1201–1218.

[15] S. A. Kulkarni, B. Li, W. K. Yip, Finite element analysis of precast hybrid-steel concrete connections under cyclic loading, Journal of constructional steel research 64 (2) (2008) 190–201.

[16] B. Li, S. A. Kulkarni, C. L. Leong, Seismic performance of precast hybrid-steel concrete connections, Journal of Earthquake Engineering 13 (5) (2009) 667–689.

[17] M. Kaya, A. S. Arslan, Analytical modeling of post-tensioned precast beam-to-column connections, Materials & Design 30 (9) (2009) 3802–3811.

[18] S. Bahrami, M. Madhkhan, F. Shirmohammadi, N. Nazemi, Behavior of two new moment resisting precast beam to column connections subjected to lateral loading, Engineering Structures 132 (2017) 808–821.

[19] D. C. Feng, G. Wu, Z. Y. Sun, J. G. Xu, A flexure-shear timoshenko fiber beam element based on softened damage-plasticity model, Engineering Structures 140 (2017) 483–497.

[20] D. C. Feng, X. D. Ren, J. Li, Softened damage-plasticity model for analysis of cracked reinforced concrete structures, Journal of Structural Engineering 144 (6) (2018) 04018044.

[21] F. J. Vecchio, M. P. Collins, The modified compression-field theory for reinforced concrete elements subjected to shear, in: ACI Journal Proceedings, Vol. 83, ACI, 1986, pp. 219–231.

[22] T. T. Hsu, Softened truss model theory for shear and torsion, ACI Structural Journal 85 (6).

[23] J. Y. Wu, J. Li, R. Faria, An energy release rate-based plastic-damage model for concrete, International Journal of Solids and Structures 43 (3) (2006) 583–612.
[24] J.-Y. Wu, J. Li, Unified plastic-damage model for concrete and its applications to dynamic nonlinear analysis of structures, Structural Engineering and Mechanics 25 (5) (2007) 519–540.
[25] J.-Y. Wu, M. Cervera, A novel positive/negative projection in energy norm for the damage modeling of quasi-brittle solids, International Journal of Solids and Structures 139 (2018) 250–269.
[26] J. Li, X. Ren, Stochastic damage model for concrete based on energy equivalent strain, International Journal of Solids and Structures 46 (11) (2009) 2407–2419.
[27] D. C. Feng, J. Li, Stochastic nonlinear behavior of reinforced concrete frames. ii: Numerical simulation, Journal of Structural Engineering 142 (3).
[28] D. C. Feng, C. Kolay, J. M. Ricles, J. Li, Collapse simulation of reinforced concrete frame structures, Structural Design of Tall & Special Buildings 25 (12) (2016) 578–601.
[29] R. Faria, J. Oliver, M. Cervera, A strain-based plastic viscous-damage model for massive concrete structures, International Journal of Solids and Structures 35 (14) (1998) 1533–1558.
[30] J. Y. Wu, Damage energy release rate-based elastoplastic damage constitutive model for concrete and its application to nonlinear analysis of structures, Phd thesis, Tongji University, Shanghai (2004).
[31] J.-Y. Wu, M. Cervera, A thermodynamically consistent plastic-damage framework for localized failure in quasi-brittle solids: Material model and strain localization analysis, International Journal of Solids and Structures 88 (2016) 227–247.
[32] D.-C. Feng, X.-D. Ren, Enriched force-based frame element with evolutionary plastic hinge, Journal of Structural Engineering 143 (10) (2017) 06017005.
[33] D.-C. Feng, J.-Y. Wu, Phase-field regularized cohesive zone model (czm) and size effect of concrete, Engineering Fracture Mechanics 197 (2018) 66–79.
[34] W.-S. Li, J.-Y. Wu, A consistent and efficient localized damage model for concrete, International Journal of Damage Mechanics 27 (4) (2018) 541–567.
[35] J. Lee, G. L. Fenves, Plastic-damage model for cyclic loading of concrete structures, Journal of engineering mechanics 124 (8) (1998) 892–900.
[36] A. Saritas, F. C. Filippou, Analysis of rc walls with a mixed formulation frame finite element, Computers and Concrete 12 (4) (2013) 519–536.
[37] D. C. Feng, X. D. Ren, J. Li, Cyclic behavior modeling of reinforced concrete shear walls based on softened damage-plasticity model, Engineering Structures 166 (2018) 363–375.
[38] L. Berto, A. Saetta, R. Scotta, D. Talledo, A coupled damage model for rc structures: Proposal for a frost deterioration model and enhancement of mixed tension domain, Construction and Building Materials 65 (2014) 310–320.
[39] M. Menegotto, Method of analysis for cyclically loaded r. c. plane frames including changes in geometry and non-elastic behavior of elements under combined normal force and bending, in: Proc.of IABSE Symposium on Resistance and Ultimate Deformability of Structures Acted on by Well Defined Repeated Loads, 1973, pp. 15–22.
[40] Effects of bond deterioration on hysteretic behavior of reinforced concrete joints.
[41] G. M. S. Alva, A. L. H. de Cresce El, et al., Moment–rotation relationship of rc beam-column connections: Experimental tests and analytical model, Engineering Structures 56 (2013) 1427–1438.
[42] D. C. Feng, G. Wu, Y. Lu, Numerical investigation on the progressive collapse behavior of precast reinforced concrete frame subassemblages, Journal of Performance of Constructed Facilities 32 (3) (2018) 04018027.
[43] G. Monti, E. Spacone, Reinforced concrete fiber beam element with bond-slip, Journal of Structural Engineering 126 (6) (2000) 654–661.
[44] S. Limkatanyu, E. Spacone, Reinforced concrete frame element with bond interfaces. i: Displacement-based, force-based, and mixed formulations, Journal of Structural Engineering 128 (3) (2002) 346–355.
[45] J. Zhao, S. Sritharan, Modeling of strain penetration effects in fiber-based analysis of reinforced concrete structures, ACI Structural Journal 104 (2) (2007) 133.
[46] W.-H. Pan, M.-X. Tao, J.-G. Nie, Fiber beam–column element model considering reinforcement anchorage slip in the footing, Bulletin of Earthquake Engineering 1–28.
[47] D.-C. Feng, J. Xu, An efficient fiber beam-column element considering flexure–shear interaction and anchorage bond-slip effect for cyclic analysis of rc structures, Bulletin of Earthquake Engineering (2018) 1–28.
[48] H. Sezen, E. J. Setzler, Reinforcement slip in reinforced concrete columns, ACI Structural Journal 105 (3) (2008) 280.
[49] J. M. Alsiwat, M. Saatcioglu, Reinforcement anchorage slip under monotonic loading, Journal of Structural Engineering 118 (9) (1992) 2421–2438.
[50] R. Costa, P. Providência, A. Dias, Anchorage models for reinforced concrete beam-column joints under quasi-static loading, ACI Structural Journal 113 (3) (2016) 503.
[51] H.-G. Kwak, J.-K. Kim, Implementation of bond-slip effect in analyses of rc frames under cyclic loads using layered section method, Engineering structures 28 (12) (2006) 1715–1727.
[52] A. Saritas, F. C. Filippou, Numerical integration of a class of 3d plastic-damage concrete models and condensation of 3d stress–strain relations for use in beam finite elements, Engineering Structures 31 (10) (2009) 2327–2336.
[53] H. Parastesh, I. Hajirasouliha, R. Ramezani, A new ductile moment-resisting connection for precast concrete frames in seismic regions: an experimental investigation, Engineering Structures 70 (2014) 144–157.